Werk

Terms and Conditions

Contact

Niedersächsische Staats- und Universitätsbibliothek Göttingen
Georg-August-Universität Göttingen
Platz der Göttinger Sieben 1
37073 Göttingen
Germany
Email: gdz@sub.uni-goettingen.de

J. Geophys. 43, 473–496, 1977

Journal of Geophysics

Lithospheric Slab Penetration into the Lower Mantle beneath the Sea of Okhotsk

T.H. Jordan

Geological Research Division, Scripps Institution of Oceanography, La Jolla, CA 92093, USA

Abstract. A set of 142 S and ScS absolute travel times and 62 ScS-S differential travel times from short-period recordings of the January 29, 1971, Sea of Okhotsk deep-focus earthquake has been analyzed to obtain estimates of the source anomaly as a function of position on the residual sphere. In the processing algorithm the station anomalies and travel times are treated as gaussian random variables with known variance matrices. A system of normal equations is found by minimizing a quadratic form that is the sum of three terms: a measure of the misfit to the absolute travel times, a measure of the misfit to the differential travel times, and a measure of the misfit to the estimated station anomalies. An approximate solution to the system of normal equations is derived by requiring that the source anomaly be a smooth function of position on the residual sphere. This fitting procedure yields a saddle-shaped source anomaly pattern. The pattern is compatible with the presence of a planar high-velocity zone beneath the source with a nearly vertical dip and a strike parallel to the Kuril-Kamchatka Arc. Ray tracing calculations have been used to model the anomaly. A high-velocity slab extending to a depth of 1000 km along the extrapolation of the Benioff Zone, with a velocity contrast of 5%, is consistent with the data. The anomaly is interpreted to be the expression of lithospheric material that has penetrated the lower mantle. This study and data from other subduction zones suggest that lithospheric slap penetration below the 650 km discontinuity is a general feature of mantle structure in regions of rapid plate convergence. It is concluded that the lower mantle participates in the thermal convection responsible for plate motions.

Key words: Subduction zones – Lower mantle heterogeneity – S-wave travel times.

1. Introduction

The fate of lithospheric material descending along subducting margins is a significant geophysical problem with important implications for mantle dy-

namics. Some authors have associated the termination of earthquake activity above 700 km depth with the equilibration of the lithospheric slab (thermal boundary layer) to ambient mantle temperatures (e.g. Toksöz et al., 1971). Others have interpreted the existence of a seismic discontinuity near 700 km and the predominance of down-dip deviatoric compressional stresses in deep-focus earthquakes to indicate the presence of a relatively high-strength mesosphere below the seismic discontinuity which is not penetrated by this thermal boundary layer (e.g. Isacks and Molnar, 1969; McKenzie et al., 1974).

Realistic thermal calculations have shown that large temperature contrasts between the slab and the surrounding mantle are likely to exist at 700 km depth for motions occurring at typical plate velocities (McKenzie, 1969; Griggs, 1972; Schubert et al., 1975), so the conclusions of Toksöz et al. (1971) are probably not well founded. But, since the thermodynamical nature of the 650-km seismic discontinuity (phase change) remains in doubt (Jackson et al., 1974; Anderson, 1976), the question of whether or not the thermal boundary layer penetrates the lower mantle cannot be categorically answered on the basis of thermal calculations alone.

However, the existence or non-existence of lower temperature lithospheric material below the seismic discontinuity can be detected by seismic methods, since this material should be characterized by higher velocities than the surrounding mantle (Davies and McKenzie, 1969; Mitronovas and Isacks, 1971; Toksöz et al., 1971; Sleep, 1973). In their study of seismic velocity anomalies beneath the Tonga-Kermadec Arc, Mitronovas and Isacks (1971, p. 7177) reported negative results: "Residuals at teleseismic distances from the deepest earthquakes show no significant azimuthal anomalies, which implies that little or no high velocity material extends beneath the deepest earthquake." Since the publication of their study, other results have become available which may reverse this conclusion. Weichert (1972), Davies and Sheppard (1972), and Powell (1976) have attributed P wave slowness anomalies observed by seismic arrays to lateral velocity gradients below the earthquake zone in the vicinity of several island arcs. Engdahl (1975) has observed travel time differences at Alaskan stations from deep-focus events in the Tonga-Fiji region which are anomalously large and which seem to require some form of velocity heterogeneity below 650 km. Jordan and Lynn (1974) have detected an anomaly in the lower mantle beneath the Middle America Trench which is characterized by high compressional and shear velocities. They suggested that this anomaly could result from low temperatures associated with down-welling material.

This evidence is compatible with the hypothesis that lithospheric material does indeed penetrate the lower mantle beneath the Benioff Zones, at least in regions where the rate of lithospheric consumption is large (Jordan, 1975). An analysis of shear wave travel times from a deep-focus earthquake in the Kuril Arc, presented here, supports this hypothesis.

2. Data

The primary observations used in this study are the distributions of S and ScS travel time residuals as functions of position on the focal sphere of a deep-focus

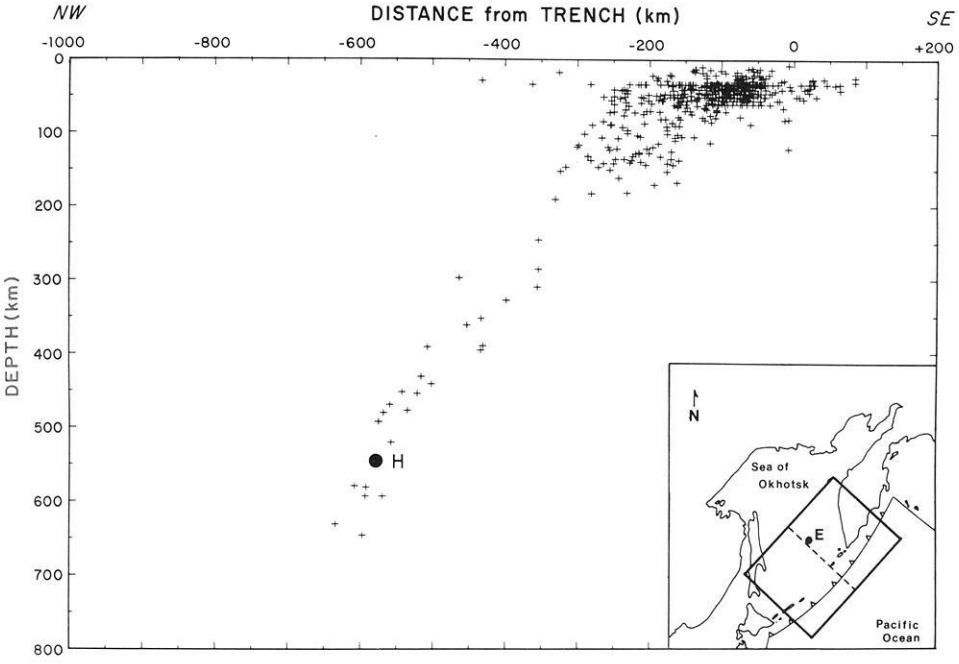

Fig. 1. Vertical cross-section perpendicular to the Kuril-Kamchatka Arc with seismicity for the period February, 1963, through April, 1974. NOAA PDE locations for events with $m_b \geqq 5$ and more than 10 stations reporting are plotted. Inset map shows region of projection (solid lines) and projection plane (dotted line). Hypocenter and epicenter of the January 29, 1971, deep-focus earthquake are indicated by *H* and *E*, respectively

event. Shear waves have been used rather than compressional waves for several reasons: (1) At a given period their wavelength is shorter by about a factor of two. Their use therefore permits a greater resolution of near-source structure. (2) The signal-to-noise ratio for ScS phases is generally much higher than for PcP phases, and, correspondingly, the travel times of ScS are more accurately determined. By employing core-reflected phases our coverage of the residual sphere is greatly increased. (3) Lower mantle heterogeneities induce variations in shear wave travel times that are generally three to four times the variations in compressional wave travel times (Jordan and Lynn, 1974).

To facilitate the accurate determination of shear-wave times on short-period recordings, an event with a simple, impulsive far-field displacement function is desired. To simplify the interpretation of the data, an accurate hypocentral location is required. The intermediate magnitude ($m_b = 6$) deep-focus Sea of Okhotsk earthquake of January 29, 1971, satisfies these criteria. Estimates of the source parameters for this event are given in Table 1. The parameter with the largest variation among the solutions listed is the focal depth: the ISC and NOAA determinations of depth differ by nearly 30 km. Fortunately, this earthquake has been relocated by Veith (1974), whose procedure incorporates station corrections and reduces network bias. He obtains a depth of 540 ± 5.7 km, which

Table 1. Estimates of Source Parameters for the January 29, 1971 Sea of Okhotsk Deep-Focus Event

Origin time	Latitude (°N)	Longitude (°E)	Depth (km)	Reference
21:58:06.7	51.72±0.032	151.04±0.024	540±5.7	Veith (1974)[a]
21:58:05.4	51.7	150.9	544	PDE[b]
21:58:03.2±0.21	51.69±0.014	150.97±0.022	515±2.7	ISC[c]
			534±1.3	pP-P times, ISC[c]

[a] Source parameters used in this paper for computing travel time residuals
[b] Preliminary Determination of Epicenters, National Oceans and Atmospheric Administration (1971)
[c] Bulletin of the International Seismological Center (1971)

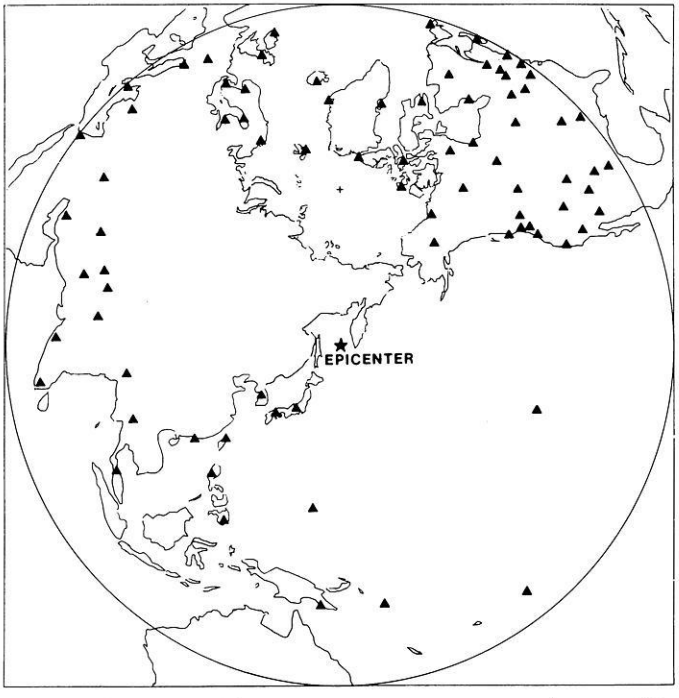

Fig. 2. Azimuthal equidistant projection centered on epicenter of January 29, 1971, deep-focus earthquake. Triangles are locations of WWSSN and Canadian Network stations used in this study. Circle is 80° from the earthquake

is consistent with the observed pP-P times (Table 1), whereas the ISC and NOAA locations are not. Veith's solution was employed in calculating travel time residuals. The location of this hypocenter is shown in the context of Benioff Zone seismicity for the Kuril-Kamchatka Arc in Figure 1.

S and ScS absolute travel times and ScS-S differential travel times were independently read from seismograms recorded at World-Wide-Standardized Seismographic Network (WWSSN) and Canadian Network stations for epicentral distances less than 80°. The station distribution is shown in Figure 2. The

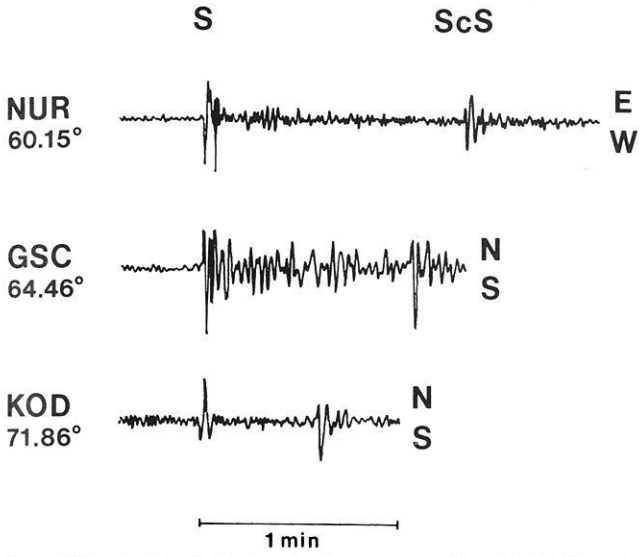

Fig. 3. Examples of short-period seismograms of S and ScS phases from the January 29, 1971, deep-focus earthquake

excellent azimuthal coverage was a primary factor in choosing this area for study. From the 80 stations where one or more measurements could be made, a total of 77 S times, 65 ScS times and 62 ScS-S times were obtained. The travel times were read from short-period seismograms for all but 4 stations, where long-period recordings were used. The arrivals were usually impulsive, and the times could generally be determined with a precision of less than one second. Examples of seismograms are shown in Figure 3. Whenever possible the times were read from the horizontal component most nearly SH-polarized. However, in some cases of poor polarization, Sp energy corrupted the S wave arrival, and identification of the first shear motion had to be made on the basis of the particle displacement.

A check on the consistency of the readings is obtained by comparing the difference between the absolute ScS and absolute S time with the independently measured ScS-S differential time. The RMS difference between these values is only 0.3 s, and the maximum difference is 0.8 s.

Residuals were formed from the raw times by subtracting the values predicted by the Seismological Tables of Jeffreys and Bullen (1940), corrected for station elevation and ellipticity. The absolute travel time residuals obtained in this manner are plotted on a stereographic projection of the focal sphere in Figure 4.

3. Residual Sphere Analysis

In seeking to explain the large variation of residuals seen in Figure 4, we will consider four factors: (1) reading errors, (2) mislocation errors, (3) failure of the

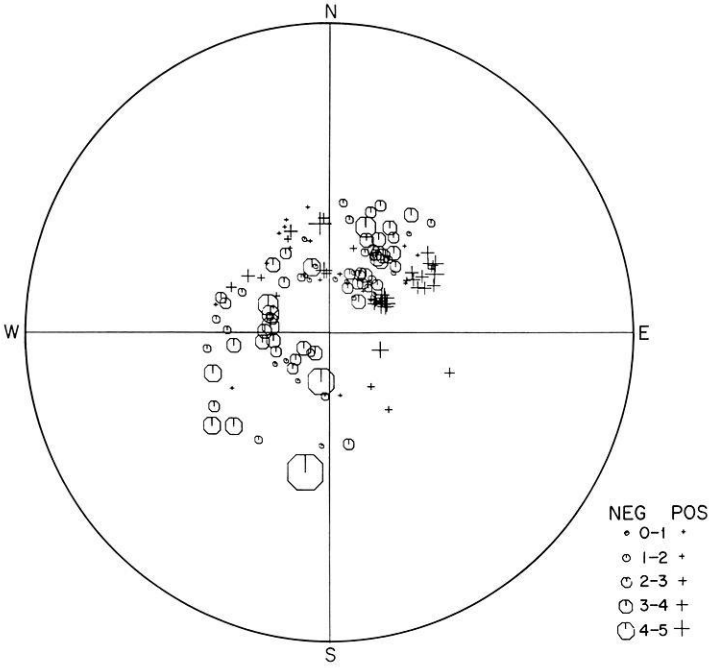

Fig. 4. Stereographic projection of lower focal hemisphere for the January 29, 1971, deep-focus earthquake showing S and ScS residuals with respect to the Jeffreys-Bullen Tables, corrected for ellipticity and station elevation. Intervals corresponding to differential symbol sizes are expressed in seconds

Jeffreys-Bullen model to adequately represent the spherically averaged earth, and (4) travel time variations due to lateral heterogeneity, The total variation exceeds 10 s, so it is unlikely that reading errors are a significant factor. Epicentral mislocation contributes to the residuals a term that varies like the cosine of the azimuth. No such systematic variation in the residuals is evident. This is not surprising since, for an epicentral uncertainty of less than 10 km, which is probably appropriate for this event, the magnitude of this term will be less than 1 s in the region sampled. Both the mislocation of focal depth and the inadequacy of the Jeffreys-Bullen model will contribute terms that are independent of azimuth. From Figure 4 it appears that variations of this type can do little to mitigate the anomalous times. For example, the average S residual and ScS residual are almost identical, -0.5 s and -0.6 s, respectively. Consequently, the bulk of the travel time variation observed in Figure 4 must be due to lateral heterogeneities in shear velocity.

Where along the ray paths do these variations occur? Inspection of Figure 4 reveals that some of the residual behavior can certainly be ascribed to anomalies in the crust and upper mantle beneath the receivers, where significant velocity heterogeneity is known to reside. For example, the largest positive residual ($+6.4$ s) is observed for the S time at Akureyri, Iceland (station AKU, azimuth $\phi = -5°$). The ScS time is also strongly positive ($+4.5$ s), and these observations

are consistent with previous inferences that the mantle beneath Iceland is characterized by low velocities (Long and Mitchell, 1970; Sipkin and Jordan, 1975). The largest negative residuals are for the S and ScS times observed at Guam (GUA, $\phi = -170°$), -10.8 s and -7.5 s, respectively. The ray paths through the upper mantle for these phases lie mostly within the lithospheric slab descending beneath the Marianas, and this geometry suggests that the large negative residuals are caused by the high velocities within the slab. Another dramatic example of near-surface anomalies can be seen in the northeastern quadrant of Figure 4: the residuals for stations in the tectonically stable regions of North America ($\phi < 50°$) are generally negative, whereas the stations in the Basin and Range Province and in western Canada ($\phi > 50°$) are invariably positive.

Since this study is primarily concerned with near-source structure, it is advantageous to eliminate these near-receiver effects as much as possible. This can be done approximately by subtracting from each residual a scalar-valued "station anomaly," determined from previous seismological experience. In a recent study by Sengupta (1975) station anomalies for most of the WWSSN stations have been derived using travel times from a global distribution of deep-focus events. Since Sengupta did not estimate anomalies for the Canadian Network, corrections for these stations were constructed on the basis of their tectonic setting, as determined from a map adapted from Douglas (1970) published by Hashizume (1976, p. 335). Stations were assigned anomalies of -2 s (shield provinces), 0 s (platforms) or $+2$ s (Phanerozoic orogens). These values are consistent with Sengupta's anomalies for other continents and with the experience of Sipkin and Jordan (1975, 1976). Based on the station's tectonic setting, anomalies were also assigned to the four WWSSN sites missing from Sengupta's catalogue: AKU, $+5.0$ s; MAT, -2.0 s; SNG, $+2.0$ s; STU, 0.0 s. Sengupta computed an anomaly of -1.6 ± 4.4 s for station GUA; to account for the observed large negative residual at this station, probably due to the slab effect mentioned above, a value of -8.0 s was substituted.

The residual sphere plot with the station anomalies removed is shown in Figure 5. Evidently, the station correction procedure has merit; the consistency of neighboring residuals is obviously improved, although the total variation in the residual magnitude is only slightly decreased. In the NW and SE quadrants the residuals are generally positive, whereas in the NE and SW quadrants the residuals are generally negative. The broad spatial coherence of this pattern suggests the existence of velocity heterogeneity in the vicinity of the source. The principal feature of this pattern is a well-defined NE-SW trending trough-like feature characterized by large negative travel time anomalies. A cross-section through the central portion of the residual distribution perpendicular to the axis of the trough is given in Figure 6. A constant baseline shift of -3 s has been added to all the residuals in Figure 6 to adjust the average anomaly for the European stations to near zero, which is consistent with the interpretation of the anomaly described below. For the portion of the residual sphere depicted in Figure 6, the amplitude of the feature is about 5 s. The magnitudes of the negative residuals increase with increasing angle from the plane of this projection. A pattern such as this can qualitatively be explained by postulating the

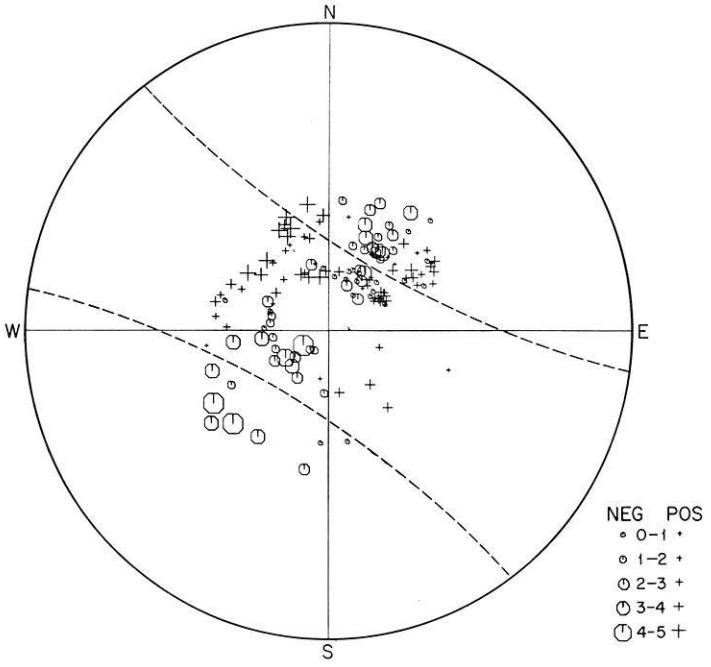

Fig. 5. Same as Figure 4, except residuals have been corrected for station anomalies discussed in the text. Dashed lines bound region of residual sphere projected in Figure 6

existence of a nearly vertically dipping high-velocity zone below the event striking parallel to the line of deep-focus earthquakes beneath the Sea of Okhotsk.

To obtain a more quantitative estimate of this near-source anomaly one can smooth the residual distribution on the focal sphere. Presumably, much of the scatter between nearby points in Figure 5 is due to reading errors or the inaccuracy of the station corrections in representing the path anomalies at large distances from the source. If nearly random as a function of position on the focal sphere, this noise can be reduced by averaging.

The procedure used in this experiment for smoothing and interpolating the residual pattern will now be outlined. To state this method most simply we must develop a compact notation. Let $\mathbf{t}_a^0$ be a vector of length N_a containing the observed absolute travel time residuals (including both the S and the ScS residuals), let $\mathbf{t}_d^0$ be a vector of length N_d containing the observed ScS-S differential travel time residuals, and let $\mathbf{t}_r^0$ be a vector of length N_r containing the observed station anomalies, taken in this instance to be Sengupta's (1975) values supplemented with the estimates of the station corrections described above. These three vectors are the experimental data at our disposal, and as such represent samples of stochastic processes. The processes will be denoted by $\mathbf{t}_a$, $\mathbf{t}_d$ and $\mathbf{t}_r$, respectively. We suppose that the quantity $\tau_s(\theta, \phi)$ represents the source anomaly for the ray leaving the hypocenter with take-off angle θ and azimuth ϕ. Let $\hat{\mathbf{r}} = (\theta, \phi)$. We shall not attempt to estimate $\tau_s(\hat{\mathbf{r}})$ directly but

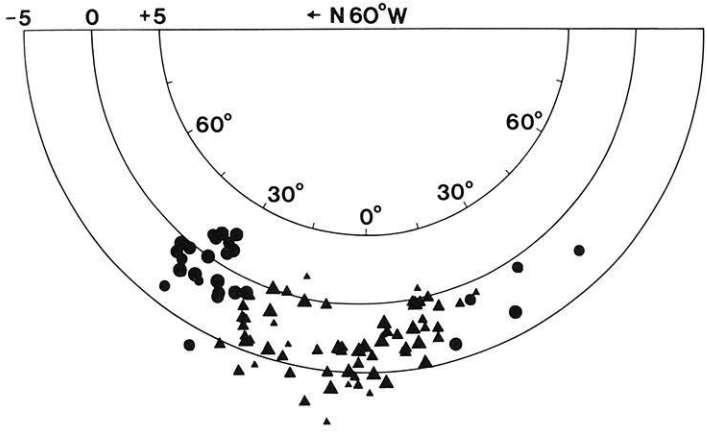

Fig. 6. Projection of the residuals bounded by dashed lines in Figure 5 onto a vertical plane through center of residual sphere oriented N60°W. Units of the radial coordinate are seconds. Circles are S times and the triangles are ScS times; size of the symbol is proportional to the subjective quality assigned to each reading. A 3 s baseline correction has been subtracted from all of the times

instead shall seek a local average of $\tau_s(\hat{\mathbf{r}})$ given by

$$t_s(\hat{\mathbf{r}}) = \int_{\mathscr{S}(1)} g(\hat{\mathbf{r}}, \hat{\mathbf{r}}')\, \tau_s(\hat{\mathbf{r}}')\, d\Omega(\hat{\mathbf{r}}') \tag{1}$$

where $\mathscr{S}(1)$ is the unit focal sphere and $g(\hat{\mathbf{r}}, \hat{\mathbf{r}}')$ is an averaging kernel that will be specified below. Let $\mathbf{t}_s$ be the vector of length N_a whose i^{th} component is $t_s(\hat{\mathbf{r}}_i)$, where $\hat{\mathbf{r}}_i = (\theta_i, \phi_i)$ is the position vector on $\mathscr{S}(1)$ of the ray corresponding to the i^{th} component of $\mathbf{t}_a$.

A very simple time-term model is assumed to be valid in the fitting procedure. For the absolute travel times we require

$$\bar{\mathbf{t}}_a = \bar{\mathbf{t}}_p + \bar{\mathbf{t}}_s \tag{2}$$

where the overbar indicates ensemble average, and the path anomaly vector $\mathbf{t}_p$ is related to the station anomaly vector by

$$\mathbf{t}_p = P \cdot \mathbf{t}_r \tag{3}$$

The operator P is an $N_a \times N_r$ matrix whose elements are

$$P_{ij} = \begin{cases} 1, & \text{if the } i^{\text{th}} \text{ path anomaly is for a ray} \\ & \text{arriving at the } j^{\text{th}} \text{ station} \\ 0, & \text{otherwise} \end{cases} \tag{4}$$

Thus, the path anomalies for the ScS and the S phases received at a given station are taken to be identical and equal to the station anomaly, an assumption necessitated by the lack of better data. The ensemble average of the differential time variable at a given station is assumed to equal the difference between the ensemble averages of the ScS variable and the S variable at that station; i.e.

$$\bar{\mathbf{t}}_d = D \cdot \bar{\mathbf{t}}_a \tag{5}$$

where D is a $N_d \times N_a$ matrix whose elements are

$$D_{ij} = \begin{cases} 1, & \text{if } t_{aj} \text{ is the ScS residual corresponding to } t_{di} \\ -1, & \text{if } t_{aj} \text{ is the } S \text{ residual corresponding to } t_{di} \\ 0, & \text{otherwise} \end{cases} \tag{6}$$

It follows that

$$D \cdot P = 0 \tag{7}$$

$$\bar{\mathbf{t}}_d = D \cdot \bar{\mathbf{t}}_s \tag{8}$$

The stochastic nature of the vectors $\mathbf{t}_a$, $\mathbf{t}_d$ and $\mathbf{t}_r$ results from experimental errors which corrupt the estimates $\mathbf{t}_a^0$, $\mathbf{t}_d^0$ and $\mathbf{t}_r^0$. The error processes are assumed to possess gaussian statistics, and the autocovariance matrices corresponding to these processes are assumed to be known. These are

$$V_{aa} = \overline{(\mathbf{t}_a - \bar{\mathbf{t}}_a)(\mathbf{t}_a - \bar{\mathbf{t}}_a)^*} \tag{9a}$$

$$V_{dd} = \overline{(\mathbf{t}_d - \bar{\mathbf{t}}_d)(\mathbf{t}_d - \bar{\mathbf{t}}_d)^*} \tag{9b}$$

$$V_{rr} = \overline{(\mathbf{t}_r - \bar{\mathbf{t}}_r)(\mathbf{t}_r - \bar{\mathbf{t}}_r)^*} \tag{9c}$$

where ( )* denotes transpose. It is convenient to assume that the errors for the components of these processes are uncorrelated; i.e. the variance matrices are taken to be diagonal. The square-roots of the diagonal elements of V_{aa} and V_{dd} measure the precision of the travel time observations. For each datum a specific value was assigned in the interval 0.5 s–2.0 s based on a subjective estimate of the datum quality. The square-root of the i^{th} diagonal element of V_{rr} was taken to be

$$(V_{rr})_{ii}^{1/2} = \begin{cases} \sqrt{\dfrac{n_i - 1}{n_i - 3}}\,\sigma_i, & \text{if } n_i > 3 \text{ and } \sqrt{\dfrac{n_i - 1}{n_i - 3}}\,\sigma_i < 4\,s \\ 4\,s, & \text{otherwise} \end{cases} \tag{10}$$

where σ_i is Sengupta's standard error of one observation at the i^{th} station and n_i is the number of observations used in his estimate. The factor $\sqrt{(n_i - 1)/(n_i - 3)}$ corrects the standard error for the increase in the uncertainty due to a finite number of observations[1]. The station corrections estimated on the basis of tectonic setting were assigned an uncertainty of 4 s.

Quantities which measure the fit of the model to the data are the quadratic forms

$$\chi_a^2 = \Delta\mathbf{t}_a^* \cdot V_{aa}^{-1} \cdot \Delta\mathbf{t}_a \tag{11a}$$

$$\chi_d^2 = \Delta\mathbf{t}_d^* \cdot V_{dd}^{-1} \cdot \Delta\mathbf{t}_d \tag{11b}$$

$$\chi_r^2 = \Delta\mathbf{t}_r^* \cdot V_{rr}^{-1} \cdot \Delta\mathbf{t}_r \tag{11c}$$

[1] Formally, this factor adjust the estimated variance to be an unbiased estimator of the second moment of the student's t distribution associated with the i^{th} datum

where

$$\Delta \mathbf{t}_a = \mathbf{t}_a^0 - \mathbf{t}_a = \mathbf{t}_a^0 - \mathbf{t}_s - P \cdot \mathbf{t}_r \tag{12a}$$

$$\Delta \mathbf{t}_d = \mathbf{t}_d^0 - \mathbf{t}_d = \mathbf{t}_d^0 - D \cdot \mathbf{t}_s \tag{12b}$$

$$\Delta \mathbf{t}_r = \mathbf{t}_r^0 - \mathbf{t}_r \tag{12c}$$

Estimates of $\mathbf{t}_s$ and $\mathbf{t}_r$ which "best fit" the data are defined as those which minimize the sum of these quadratic forms

$$\chi_T^2 = \chi_a^2 + \chi_d^2 + \chi_r^2 \tag{13}$$

Minimizing χ_T^2 with respect to arbitrary variations in $\mathbf{t}_s$ and $\mathbf{t}_r$ is accomplished with equations (11) and (12) and standard variational techniques. It can be shown that a minimum is attained when the estimates $\tilde{\mathbf{t}}_s$ and $\tilde{\mathbf{t}}_r$ satisfy the following system:

$$[V_{aa}^{-1} + D^* \cdot V_{dd}^{-1} \cdot D] \cdot \tilde{\mathbf{t}}_s + V_{aa}^{-1} \cdot P \cdot \tilde{\mathbf{t}}_r = V_{aa}^{-1} \cdot \mathbf{t}_a^0 + D^* \cdot V_{dd}^{-1} \cdot \mathbf{t}_d^0 \tag{14a}$$

$$P^* \cdot V_{aa}^{-1} \cdot \tilde{\mathbf{t}}_s + [P^* \cdot V_{aa}^{-1} \cdot P + V_{rr}^{-1}] \cdot \tilde{\mathbf{t}}_r = P^* \cdot V_{aa}^{-1} \cdot \mathbf{t}_a^0 + V_{rr}^{-1} \cdot \mathbf{t}_r^0 \tag{14b}$$

Since V_{rr} is nonsingular, the matrix

$$R \equiv P^* \cdot V_{aa}^{-1} \cdot P + V_{rr}^{-1} \tag{15}$$

will also be nonsingular and thus possess an inverse. Equation (14b) can therefore be solved for $\tilde{\mathbf{t}}_r$ in terms of $\tilde{\mathbf{t}}_s$:

$$\tilde{\mathbf{t}}_r = R^{-1} \cdot [P^* \cdot V_{aa}^{-1} \cdot \mathbf{t}_a^0 + V_{rr}^{-1} \cdot \mathbf{t}_r^0 - P^* \cdot V_{aa}^{-1} \cdot \tilde{\mathbf{t}}_s] \tag{16}$$

Substituting (16) into (14a) we find

$$S \cdot \tilde{\mathbf{t}}_s = \mathbf{d}^0 \tag{17}$$

where

$$S \equiv V_{aa}^{-1} + D^* \cdot V_{dd}^{-1} \cdot D - V_{aa}^{-1} \cdot P \cdot R^{-1} \cdot P^* \cdot V_{aa}^{-1} \tag{18a}$$

$$\mathbf{d}^0 \equiv [V_{aa}^{-1} - V_{aa}^{-1} \cdot P \cdot R^{-1} \cdot P^* \cdot V_{aa}^{-1}] \cdot \mathbf{t}_a^0 + D^* \cdot V_{dd}^{-1} \cdot \mathbf{t}_d^0 - V_{aa}^{-1} \cdot P \cdot R^{-1} \cdot V_{rr}^{-1} \cdot \mathbf{t}_r^0 \tag{18b}$$

Thus, minimizing (13) can be reduced to the problem of solving an $N_a \times N_a$ system of linear equations. Because the matricies P and D are simple and because the variance matricies (9) are taken to be diagonal, the matrix multiplications in (16), (18a) and (18b) can be done analytically, and Equations (16) and (17) are easily set up for numerical computations.

For the problem at hand, the euclidean norm of the last term in expression (18a) exceeds the euclidean norm of the sum of the first two terms, and the matrix S may be singular. Furthermore, the ratio of largest eigenvalue to the smallest nonzero eigenvalue of the matrix $S^2 = S^* \cdot S$ is very large, and hence the computation of the generalized inverse of S is an ill-posed problem.

Fortunately, the manifold of exact solutions to the normal equations (17) is of little interest. Our concern is the construction of the smoothest approximate

solution which satisfies the observational constraints to our satisfaction. To do this let us return to Equation (1), where the elements of $\mathbf{t}_s$ were defined to be the convolution of the source anomaly $\tau_s(\hat{\mathbf{r}}')$ with a smoothing kernel $g(\hat{\mathbf{r}}, \hat{\mathbf{r}}')$. We now specify this kernel to be

$$g(\hat{\mathbf{r}}, \hat{\mathbf{r}}') = \frac{\exp[\kappa \hat{\mathbf{r}} \cdot \hat{\mathbf{r}}']}{4\pi q_0(\kappa)} \tag{19}$$

where $q_0(\kappa) \equiv \sinh(\kappa)/\kappa$. These kernels are simply unimodular versions of Fisher's fundamental distribution on $\mathscr{S}(1)$, and with this specification, Equation (1) represents the convolution of τ_s with the spherical equivalent of a gaussian filter function. The filter is low-pass, and the parameter κ controls the filter width. Define $\mathbf{G}(\hat{\mathbf{r}}')$ to be the vector of length N_a whose i^{th} element is $g(\hat{\mathbf{r}}_i, \hat{\mathbf{r}}')$, where $\hat{\mathbf{r}}_i$ is the position on $\mathscr{S}(1)$ of the ray corresponding to the i^{th} element of $\mathbf{t}_a$. Define C_{ss} to be the $N_a \times N_a$ matrix

$$C_{ss} = \int_{\mathscr{S}(1)} \mathbf{G}(\hat{\mathbf{r}})\, \mathbf{G}^*(\hat{\mathbf{r}})\, d\Omega(\hat{\mathbf{r}}) \tag{20}$$

The elements of C_{ss} are easily shown to be

$$C_{ss}(\hat{\mathbf{r}}_i, \hat{\mathbf{r}}_j) = \frac{q_0(\kappa[2 + 2\hat{\mathbf{r}}_i \cdot \hat{\mathbf{r}}_j]^{1/2})}{4\pi q_0^2(\kappa)} \tag{21}$$

for $i, j = 1, 2, \ldots, N_a$. Let $\boldsymbol{\psi}^{(m)}$ be the eigenvector of $S \cdot C_{ss} \cdot S^*$ corresponding to the eigenvalue $\lambda^{(m)}$:

$$(S \cdot C_{ss} \cdot S^*) \cdot \boldsymbol{\psi}^{(m)} = \lambda^{(m)} \boldsymbol{\psi}^{(m)}, \qquad m = 1, \ldots, N_a \tag{22}$$

Since C_{ss} is a positive semi-definite symmetric matrix, the eigenvalues $\lambda^{(m)}$ are positive or zero, and the eigenvectors can be constructed to be orthonormal. We suppose that the eigenvalues are arranged in decreasing order of magnitude:

$$\lambda^{(1)} \geqq \lambda^{(2)} \geqq \cdots \geqq \lambda^{(m)} \geqq \cdots \geqq \lambda^{(N_a)} \geqq 0$$

For $M \leqq N_a$, define the dyad

$$T^{(M)} = \sum_{m=1}^{M} (\lambda^{(m)})^{\dagger}\, \boldsymbol{\psi}^{(m)}\, \boldsymbol{\psi}^{*(m)} \tag{23}$$

where $(\ )^{\dagger}$ denotes the generalized inverse;

$$(\lambda^{(m)})^{\dagger} = \begin{cases} (\lambda^{(m)})^{-1}, & \text{if } \lambda^{(m)} > 0 \\ 0, & \text{if } \lambda^{(m)} = 0 \end{cases} \tag{24}$$

As approximate solutions to (17) consider the sequence

$$\tilde{\mathbf{t}}_s^{(M)} = C_{ss} \cdot S^* \cdot T^{(M)} \cdot \mathbf{d}^0; \qquad M = 1, \ldots, N_a \tag{25}$$

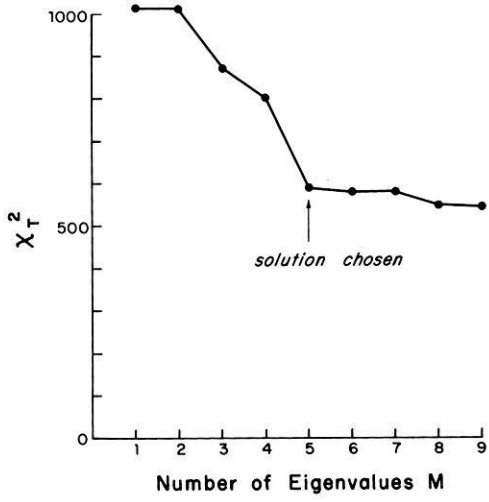

Fig. 7. Plot of the dimensionless fitting parameter χ_T^2, as a function of the number of eigenvectors incorporated into the solution given by Equation (25)

For each $M \leqq N_a$, $[\chi_T^2]^{(M)}$, the value of the fitting parameter (13), can be computed. Several properties of these sequences are noted:

(i) $T^{(N_a)}$ is simply the generalized inverse of $S \cdot C_{ss} \cdot S^*$, and $\tilde{\mathbf{t}}_s^{(N_a)}$ $= C_{ss} \cdot S^* \cdot (S \cdot C_{ss} \cdot S^*)^\dagger \cdot \mathbf{d}^0$ is the solution to (17) which minimizes the Riemannian norm $[\mathbf{t}_s^* \cdot C_{ss}^{-1} \cdot \mathbf{t}_s]^{1/2}$ (assuming C_{ss}^{-1} exists).

(ii) With C_{ss} specified by a smoothing operator, the sequence of solutions is ordered such that $\tilde{\mathbf{t}}_s^{(M)}$ is "smoother" than $\tilde{\mathbf{t}}_s^{(M')}$ if $M < M'$ and if the eigenvalues $\lambda^{(M)}$ and $\lambda^{(M')}$ are distinct. (See Jordan and Minster (1971, p. 7–42) for the precise definition of smoothness used here.)

(iii) $[\chi_T^2]^{(M)}$ is a monotonically decreasing function of M.

Thus, as M increases, more character (roughness) is added to the solution and the fit to the data is improved. As M approaches N_a, the solution approaches a generalized inverse solution.

Our procedure is to find the smallest value of M such that increasing M does not significantly reduce χ_T^2.

In the calculations, the value $\kappa = 2.8$ has been chosen. The associated filter half-width is given by

$$\Delta(\kappa) = \cos^{-1}(1 - \kappa^{-1}) \simeq 0.873 \text{ radians} \tag{26}$$

or about 50°. Numerical experiments demonstrate that the solution yielded by the algorithm is not very sensitive to the value of κ. The solution sequence (25) has been computed for $1 \leqq M \leqq 9$, and the corresponding values of χ_T^2 are plotted as a function of M in Figure 7. The value of the fitting function decreases markedly out to $M = 5$. For $M > 5$, the decrease in χ_T^2 upon adding additional eigenvectors is very small. This behavior was checked by computing the solution for $M = 30$; the concomitant value of χ_T^2 still exceeded 500. Therefore, no

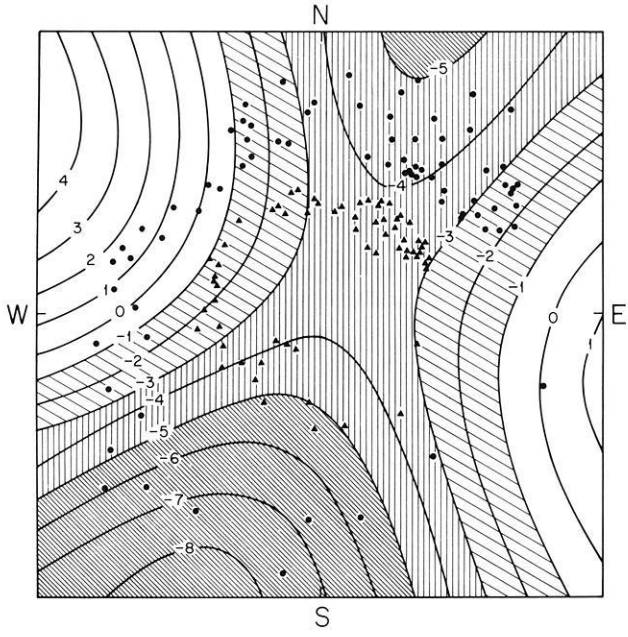

Fig. 8. Stereographic projection of a portion of the lower focal hemisphere with source anomaly contours computed from Equation (27) for $M=5$. Contour interval is 1 s. Locations of S and ScS rays corresponding to observed absolute travel times are represented by circles and triangles, respectively. Region depicted is portion of the lower hemisphere shaded in figure at lower right. Baseline correction is the same as in Figure 6

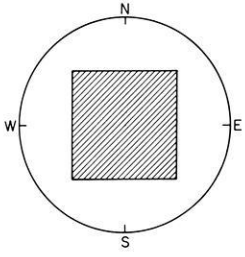

significant improvement in the fit to the data is achieved by increasing M beyond 5, and the structure introduced by adding more eigenvectors is not required by the data.

The smoothed source anomaly computed for $M=5$ is shown in Figure 8. The solution vector has been interpolated by the formula

$$\tilde{t}_s^{(M)}(\hat{\mathbf{r}}) = \int_{\mathscr{S}(1)} g(\hat{\mathbf{r}}, \hat{\mathbf{r}}')\, \mathbf{G}^*(\hat{\mathbf{r}}') \cdot S^* \cdot T^{(M)} \cdot \mathbf{d}^0\, d\Omega(\hat{\mathbf{r}}'); \qquad \hat{\mathbf{r}} \in \mathscr{S}(1) \tag{27}$$

The fact that the solution vector is easily interpolated in a manner consistent with the smoothing, without the need for imposing further structure, is an advantage of the method. Figure 8, the principal product of the data analysis, is discussed at length below.

The fit of the model to the data is shown in Figure 9, which displays the distribution histograms of the residuals defined by Equations (12) normalized by their assigned standard deviations for each of the three data types. The fit to the absolute travel times and the station anomalies is good, with respectively 70% and 81% of the data lying within one standard deviation of the computed values, compared with an expected 67%. The fit to the differential travel times is less good: only 44% of the data lie within one standard deviation of the computed values. The poorness of this fit has a simple explanation. In the analysis we have taken the errors in the differential travel times and the errors in the absolute travel times to be equal (if the subjective qualities assigned to the picks were the same) and uncorrelated. Although that part of the uncertainty in the ScS-S times caused by reading errors may approximate this behavior (the readings were made independently), any errors arising from incorrect assump-

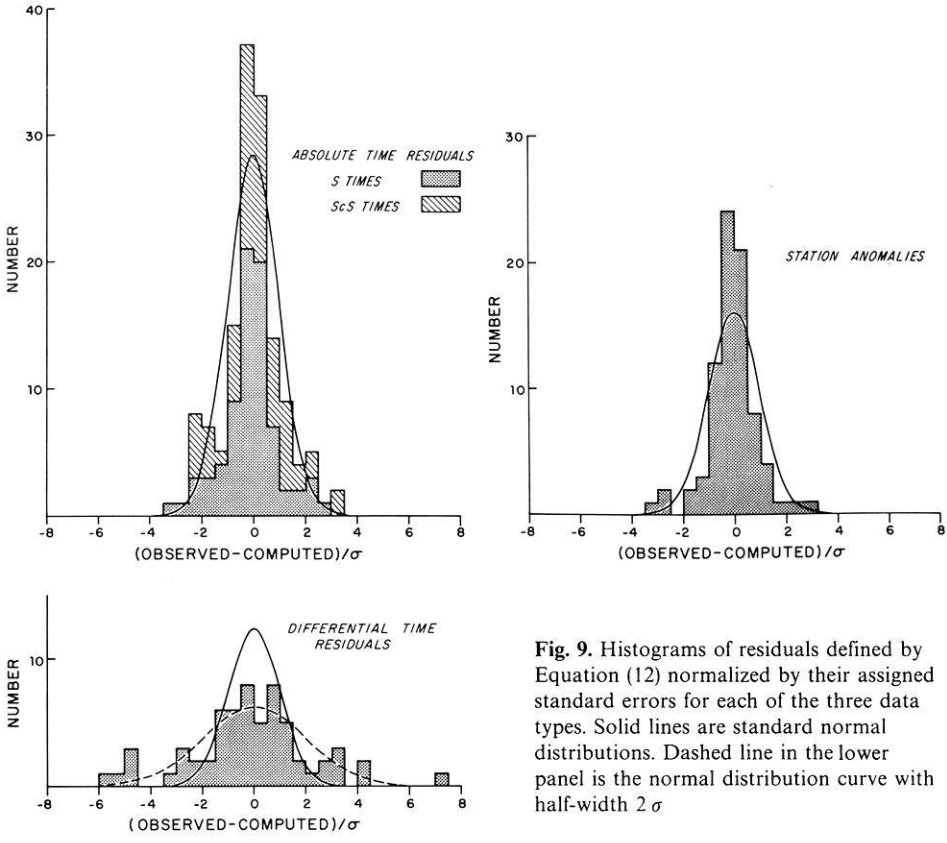

Fig. 9. Histograms of residuals defined by Equation (12) normalized by their assigned standard errors for each of the three data types. Solid lines are standard normal distributions. Dashed line in the lower panel is the normal distribution curve with half-width 2σ

tions in the formulation of the model surely do not. For example, representation of the path anomalies in terms of a station correction that is identical for both S and ScS is probably a crude approximation. The errors in the ScS-S times due to the incorrectness of this assumption can be expected to equal nearly the sum of the associated errors in the S and ScS times and are thus correlated with the errors in the absolute times. If this is the dominant source of error and if these errors in the absolute times are themselves uncorrelated, then the variance of the differential time residuals should be approximately twice the variance of the absolute time residuals. The observation that the differential and absolute travel times are internally consistent, discussed in the previous section, suggests that correlated errors of this sort do dominate, and the standard deviations of the ScS-S times should therefore be increased by a factor of $\sqrt{2}$. If this is done, 62% of the observed differential travel times fall within one standard deviation of the computed values, which is an adequate fit to the data.

The fact that the noise in the differential travel times is correlated with the noise in the absolute times explains why the model value of χ_T^2 is large (545). If the data processes were uncorrelated (e.g. $V_{ad}=0$), then χ_T^2 would be chi-square

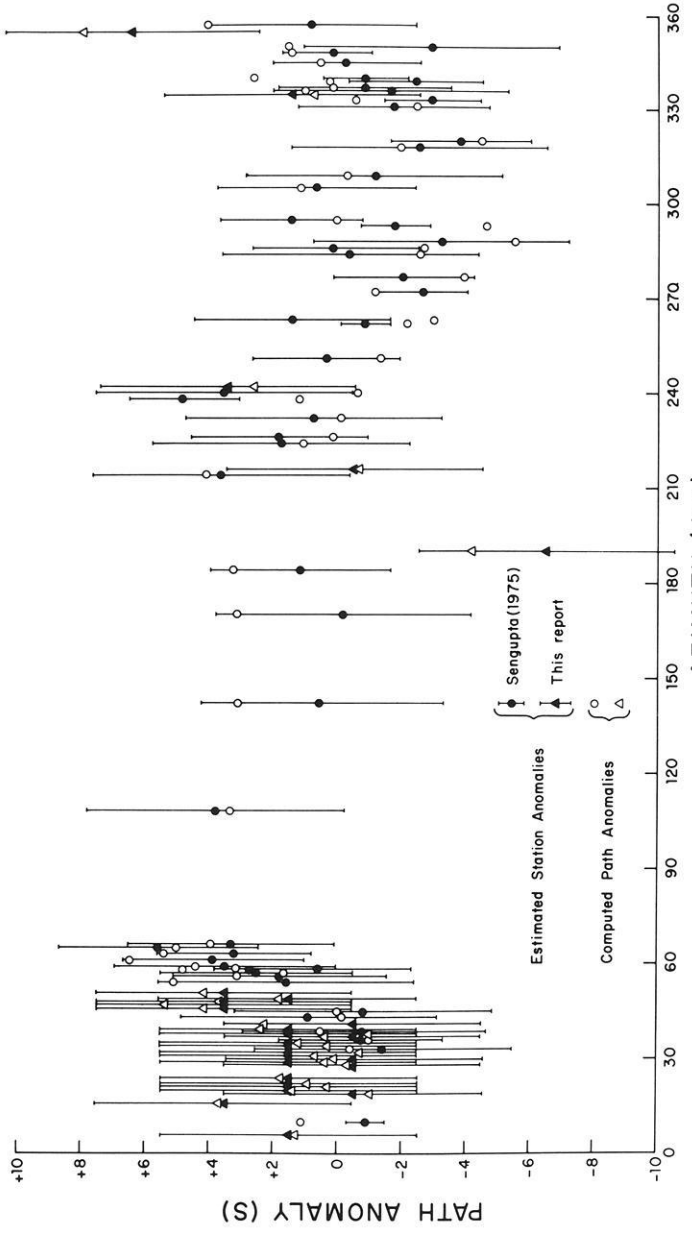

Fig. 10. Estimated station anomalies and computed path anomalies ($M=5$) as a function of azimuth from the source. Error bars indicate assigned standard errors. An arbitrary baseline shift of +1.5 s has been added to all quantities

distributed with $v=199$ degrees of freedom (284 data constraining 80 station corrections and 5 source anomaly parameters), and a model with $\chi_T^2 > v + 1.65\sqrt{2v} \simeq 232$ could be rejected with only a 5% chance of making a type I error. However, since these statistical assumptions are incorrect, the model cannot be rejected on this basis.

A more detailed comparison of the station corrections $\tilde{\mathbf{t}}_r$ (path anomalies) computed from equation (16) using $\tilde{\mathbf{t}}_s^{(5)}$ and the estimated station corrections $\mathbf{t}_r^0$ is made in Figure 10, which plots these quantities as a function of azimuth from the source. As was stated above, the fit is good, considering the large uncertainties associated with $\mathbf{t}_r^0$, and there is no bias evident in the distribution shown at the bottom of Figure 9. However, when viewed as a function of azimuth, the variations in $\Delta t_r = t_r^0 - \tilde{t}_r$ are systematic. For stations in the Basin and Range Province, the Pacific Ocean and western Europe, Δt_r is generally positive, whereas, for stations in Canada, India and Asia, this difference is generally negative. A comparison of Figures 8 and 10 shows that the systematic variation in the fit to the station correction data mimics the computed source anomaly. The effect of decreasing this bias as a function of azimuth would be to increase the magnitude of the source anomaly in Figure 8 without changing its basic pattern. This is an artifact of the method, which finds the shortest solution (in the sense of the Riemannian norm discussed under point (i) above) that minimizes χ_T^2. It is a desirable feature of the solution in the sense that the amplitude of the source anomaly is probably underestimated, rather than overestimated.

4. Interpretation

A convincing way to verify the smoothing and interpolation algorithm is simply to compare Figures 5 and 8: processing the data by eye agrees well with processing the data by computer. In making this comparison, one should note that a baseline shift of -3 s has been applied to the source anomaly in Figure 8. The "real" source anomaly baseline is not usefully constrained by this experiment, because the baseline for the station corrections is essentially arbitrary and because there exists a trade-off between the average source anomaly and the origin time of the source. Of course, in discussions of velocity contrasts, the particular choice of the baseline is unimportant. It is significant only when we attempt to relate the source anomaly to absolute velocities, say, those of the spherically averaged earth.

I interpret the source anomaly derived from this earthquake to be the expression of a high-velocity zone beneath the source which is extended parallel to the Benioff Zone. Accordingly, the baseline in Figure 8 has been chosen to yield a nearly zero anomaly for S rays which leave the source at shallow angles in the NW direction (to European stations), the same baseline used in Figure 6.

The topographic form of the anomaly is consistent with this interpretation. It is saddle-shaped with nearly perpendicular axes centered roughly in the middle of the focal sphere. The axis of the "valleys" is oriented approximately parallel to the strike of the Benioff Zone. With the chosen baseline, the anomaly at the center of the saddle is about -3.5 s. If the material beneath the source has shear velocities higher than the surrounding mantle by 5%, say, then this material has to extend to a depth of nearly 1000 km to produce the stated decrease in travel time. To reduce the depth extent of this material, the velocity contrast must be increased correspondingly.

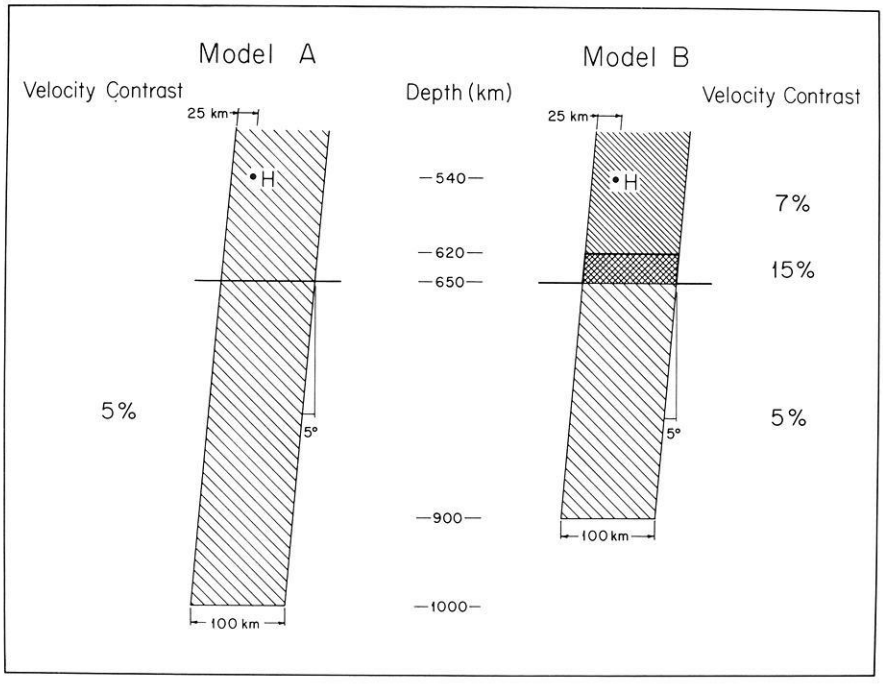

Fig. 11. Vertical cross-sections along azimuth N60°W through preliminary models of the lower mantle anomaly beneath the Sea of Okhotsk used in computing the diagrams in Figure 12. Structure is uniform in direction perpendicular to section and is imbedded in a spherically symmetric earth model. H represents hypocenter location relative to structure

In an attempt to obtain a more detailed picture of the anomalous mantle below this earthquake, a number of parameterized models have been formulated, and their theoretical anomaly patterns have been generated by a simple ray tracing algorithm. In the algorithm the velocities of the Jeffreys-Bullen model are approximated by a circular ray distribution (Bullen, 1963, p. 122), and the source anomaly is computed by integrating the slowness contrasts along the ray paths. As a consequence of Fermat's Principle, this procedure yields travel time anomalies correct to first order in the contrasts, but no accounting for ray path distortion is made. Hence, the theoretical anomalies are mapped onto the focal sphere incorrectly, and the computed anomaly pattern is distorted. For typical slab structures the distortion can be quite severe (c.f. Toksöz et al., 1971, p. 1129). However, the "observed" anomaly pattern in Figure 8 was generated from travel times mapped onto the focal sphere also using a spherically symmetric model. Thus, the approximations are self-consistent and are hopefully valid for the purposes of a qualitative comparison. But, certainly, any results based on them must be considered tentative until they are verified by more exact three-dimensional calculations.

Two models of the anomalous mantle are shown in Figure 11. Both are slab-like structures 100 km thick of uniform lateral extent striking N30°E with a dip

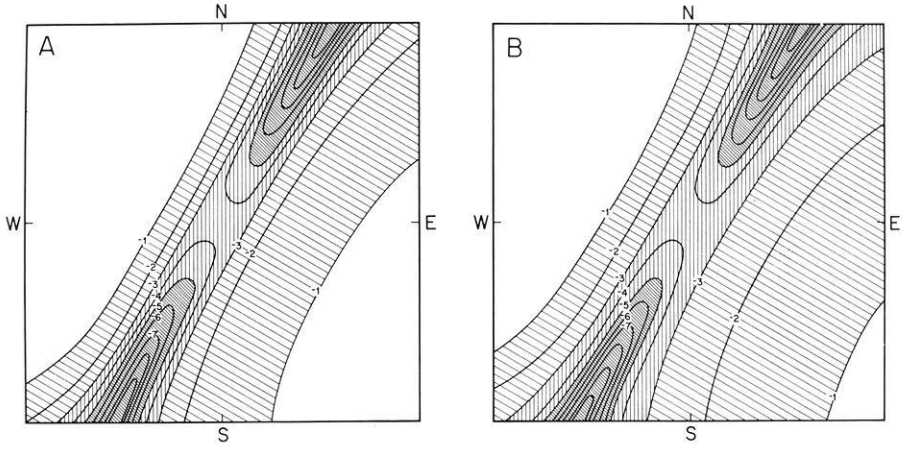

Fig. 12. Stereographic projections of a portion of the lower focal hemisphere with source anomaly contours computed from models A and B (Fig. 11). Contour interval is 1 s. Method of computation is approximate and does not include the effects of perturbations to the ray paths caused by the anomalous structure

of 85° in the N60°W direction. In model A the velocity contrast is a constant 5% and the slab continues below the hypocenter to a depth of 1000 km. In model B the velocity contrast varies discontinuously down the slab to a depth of 900 km. The region of high velocity contrast (+15%) in model B is designed to represent a 30-km elevation of the mantle discontinuity (phase change) near 650 km, a possibility which is discussed further below. The source anomaly patterns calculated for these models are shown in Figure 12.

These patterns are quite similar, indicating that the data are not very sensitive to the trade-off between slab length and average velocity contrast. For both models the variation qualitatively matches the saddle-shaped source anomaly derived from the data. The calculations were made with the hypocenter located 25 km from the NW boundary of the slab. This location should be near the coolest part of the slab (Schubert et al., 1975) where, at shallower depths, most of the seismicity is concentrated (Engdahl, 1973; Veith, 1974). Choosing the location of the source to be nearer the NW side of the slab introduces an asymmetry about one axis of the saddle, increasing the gradient along northwesterly azimuths and decreasing the gradient along southeasterly azimuths. Interestingly, such an asymmetry in these gradients is evident in Figures 6 and 8.

An asymmetry about the other axis of the saddle-shaped source is also present: the SW valley is deeper and more pronounced than the NE valley. Limiting the slab's lateral dimension from the source to several hundred kilometers in the NE direction can quantitatively explain the asymmetry. This explanation is plausible, because the deep-focus seismicity terminates about 400 km northeast of the source beneath the Kamchatka Peninsula, near its intersection with the Aleutian Arc transform fault. (To the southwest the geometry of the Benioff Zone is essentially unchanged to the Hokkaido Corner, over 1000 km distant from the source.)

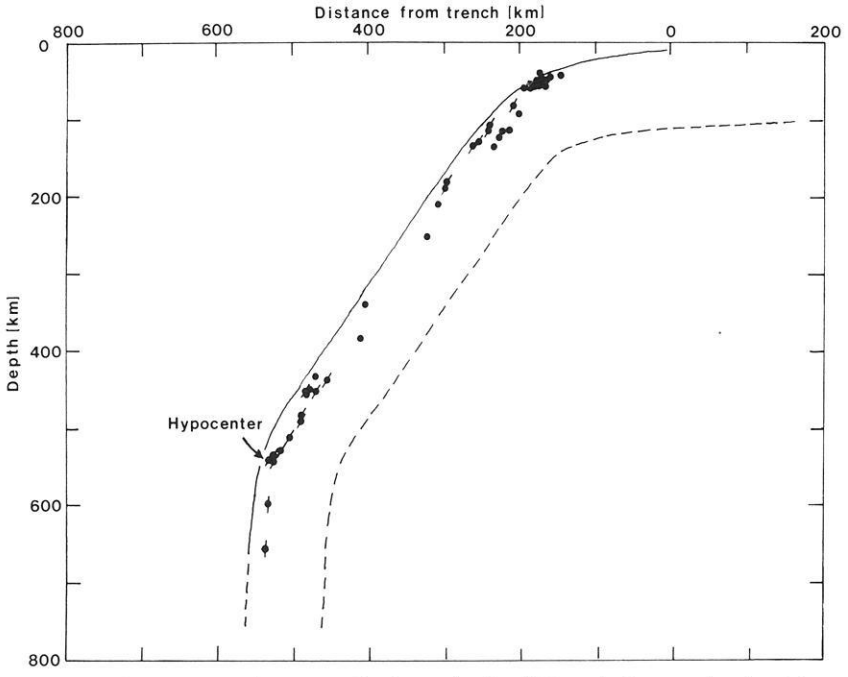

Fig. 13. Vertical cross-section perpendicular to the Kuril-Kamchatka Arc showing inferred location of descending lithospheric material above the seismic discontinuity (after Veith, 1974, pp. 31–32, sections 9 and 10). Black dots are relocated hypocenters and short line segments represent orientation of compressional axes for events with down-dip compression. Note the inferred change in the dip of the Benioff Zone near 550 km depth. The hypocenter of the January 29, 1971, earthquake is indicated by the arrow

These explanations for the source anomaly asymmetry in terms of the slab geometry are appealing, but, despite their plausibility, neither is really demanded by the data. For the existence of the asymmetries to be required, the extrapolation of the source anomaly to regions of the focal sphere outside the data range ($\theta > 52°$) and its interpolation in regions where the data are sparse (e.g. the SE quadrant) must be trusted. Any such trust is misplaced, since the anomaly values within these regions are very uncertain. Furthermore, the asymmetry in Figure 8 can largely be removed by postulating that the source is mislocated 0.15°ENE of the actual epicenter. Although an epicentral mislocation of this magnitude is considered unlikely, it cannot be discounted as an alternate hypothesis.

A notable discrepancy between the estimated anomaly pattern and the theoretical calculations is the broadness of the negative valleys in Figure 8 compared with those in Figure 12. This could be evidence that the effective slab width exceeds the model value of 100 km, but, again, explanations independent of the slab structure are possible. Perhaps the data have been smoothed too much; a narrower negative trough is certainly not excluded by the data in Figure 5. Also, the effects of residual sphere distortion by the three-dimensional structure, which could contribute to the broadening, remain to be evaluated.

One feature of the model which does appear to be required by the data is the near vertical dip of the high-velocity zone beneath the source. Decreasing the dip to much less than 80° distorts the anomaly pattern severely and predicts larger negative residuals for the ScS-S times at stations in western Europe than are observed. This nearly vertical dip was at first surprising to the author, since the dip of the Benioff Zone above the event is close to 45° (Fig. 1). Figure 1 does indicate, however, that the dip of the seismic zone may change at a depth of about 550 km. Evidence supporting this hypothesis was obtained independently and prior to this study by Veith (1974), whose results are summarized in Figure 13. Not only do his relocated hypocenters indicate this change in dip, but there is a distinct, similar change in the orientation of compressional axes at about 550 km depth. This independent evidence for the nearly vertical dip of the slab below the hypocenter adds weight to our results.

5. Discussion

The data base and modelling procedures used here are too crude to place bounds on the depth extent of the high-velocity material without the incorporation of further constraints, such as a bound on the maximum velocity contrasts. Mitronovas and Isacks (1971) have estimated the average shear velocity contrasts within the slab above the deep-focus zone to be $7\% \pm 1\%$, a value compatible with the observed compressional velocity contrasts. Higher lateral velocity contrasts, perhaps as great as 15%, could exist in a limited depth range if the 650-km mantle discontinuity were elevated because of reduced temperatures within the descending lithospheric slab. If the temperature contrasts are as great as 700 °C, as in the model of Schubert et al. (1975), and the Clapeyron slope for the 650-km phase transition is as great as 2×10^{-2} Kb/°C, then this discontinuity could be elevated as much as 30 km. These assumptions are incorporated into model B and imply a minimum depth extent for the high velocity material of 900 km. However, best estimates of the entropy change across the 650-km transition are near zero (Jackson et al., 1974; Anderson, 1976), so little or no change in the depth of this discontinuity is expected, regardless of the temperatures. Furthermore, the predicted temperature contrasts below 400 km are lower by several hundred degrees than at shallower depths, due to conductive heating and some warming by exothermic reactions (Schubert et al., 1975); thus, the velocity contrasts beneath the source are likely to be less than 7%. If so, the depth extent of the high-velocity material probably exceeds 900 km, as in model A.

It should be noted that these depth estimates are lower bounds, since small scale lateral heterogeneity below 900 km depth subtends only small solid angles from a deep-focus source, and its expression in the focal sphere anomaly pattern will not be observable. Also, more realistic three-dimensional ray tracing calculations may reduce somewhat the large negative anomalies shown in Figure 12.

Thus, a zone of high-velocity material extends well into the lower mantle beneath the Kuril-Kamchatka subduction zone. Similar anomalies apparently

exist beneath other regions of plate convergence, and I interpret these features to be the expressions of colder lithospheric material that has penetrated the lower mantle (Jordan, 1975). This evidence strongly supports the old hypothesis that the lower mantle participates in thermal convection (Jordan, 1975; O'Connell, 1976; Davies, 1976), at least the large-scale flow responsible for plate motions (Richter and Parsons, 1975).

6. Conclusions

(a) An algorithm has been formulated for recovering the source anomaly by smoothing and interpolating travel time data which densely populate a region of the focal sphere. The algorithm is based on standard least-squares analysis, but some of the specific methods discussed here may be usefully applied elsewhere.
(b) Application of the algorithm to shear-wave travel time data from the January 29, 1971, Sea of Okhotsk deep-focus earthquake yields a saddle-shaped source anomaly pattern (Fig. 8). This pattern is compatible with the presence of a planar high-velocity zone beneath the source with a nearly vertical dip and a strike parallel to the Kuril-Kamchatka Arc. The high-velocity zone is interpreted to be the expression of colder lithospheric material that has penetrated the mantle below the seismic discontinuity near 650 km.
(c) The configuration of the high-velocity zone has been explored by a simple ray-tracing method which predicts, to first order, the magnitude of the travel time anomalies associated with lateral structure but does not account for ray path distortion. These calculations indicate that the dip of the high-velocity zone is greater than 80°. This agrees with the geometry of the slab at depths greater than 550 km deduced by Veith (1974) from a study of seismicity and fault plane solutions. Asymmetries in the derived anomaly pattern can be explained by locating the source near the northwestern boundary of the slab and by limiting the slab's northeastern extent, hypotheses which are also compatible with the geometry of the seismic zone. However, these asymmetries are only marginal features of the solution and, even if significant, may be caused by source mislocation. The broadness of the negative valleys in Figure 8 may indicate that the effective width of the slab is greater than the model value of 100 km, but, again, explanations independent of mantle structure are tenable. A bound on the depth extent of the high-velocity zone is possible only if additional constraints are imposed. If the 650-km discontinuity is unperturbed by the presence of the anomalous temperatures and if the average shear velocity contrast is 5% or less, then the high-velocity material must extend to at least 1000 km depth to account for the anomalous times. High velocities may exist at greater depths, but the data do not resolve this deeper structure. The conclusions concerning the configuration of the anomalous zone are tentative until more realistic three-dimensional ray tracing calculations are applied to this data set. The modelling attempted here should be considered as only the first step of an iterative procedure aimed at explaining the data.
(d) This study and other work on mantle heterogeneity strongly suggest that material is being exchanged between the upper mantle and the lower mantle

and, thus, that the convection implied by plate motions is not confined to the upper mantle.

Acknowledgements. Gratitude is expressed to R. Strelitz for bringing Veith's (1974) work to the author's attention and to K. Veith for allowing quotations from his unpublished thesis, especially the information in Figure 13. S. Sipkin and K. Sverdrup assisted in the computations. This research was sponsored by the National Science Foundation under grant EAR75-20993.

References

Anderson, D.L.: The 650 km mantle discontinuity. Geophys. Res. Lett. **3**, 347–349, 1976

Bullen, K.E.: Introduction to the theory of seismology, 3rd ed. Cambridge: Cambridge University Press 1963

Davies, D., McKenzie, D.P.: Seismic travel-time residuals and plates. Geophys. J. Roy. Astr. Soc. **18**, 51–63, 1969

Davies, D., Sheppard, R.M.: Lateral heterogeneity in the Earth's mantle. Nature **239**, 318–323, 1972

Davies, G.F.: Whole mantle convection and plate tectonics. Submitted for publication, 1976

Douglas, R. J. W. (ed.): Geology and economic minerals of Canada. Ottawa, Ont.: Dept. Energy, Mines and Resources, p. 3 and pp. 44–150, 1970

Engdahl, E.R.: Relocation of intermediate depth earthquakes in the Central Aleutians by seismic ray tracing. Nature **245**, 23–25, 1973

Engdahl, E.R.: Effects of plate structure and dilatancy on relative teleseismic P-wave residuals. Geophys. Res. Lett. **2**, 420–422, 1975

Griggs, D.T.: The sinking of the lithosphere and the focal mechanism of deep earthquakes. In: The nature of the solid earth (E. C. Robertson, ed.), pp. 361–384. New York: McGraw-Hill 1972

Hashizume, M.: Surface-wave study of the Canadian Shield. Phys. Earth Planet. Int. **11**, 333–351, 1976

International Seismological Centre: Bulletin, Edinburgh, 1971

Isacks, B., Molnar, P.: Mantle earthquake mechanisms and the sinking of the lithosphere. Nature **223**, 1121–1124, 1969

Jackson, I.N.S., Liebermann, R.C., Ringwood, A.E.: Disproportionation of spinels to mixed oxides: significance of cation configuration and implications for the mantle. Earth Planet. Sci. Lett. **24**, 203–208, 1974

Jeffreys, H., Bullen, K.E.: Seismological Tables. British Association for the Advancement of Science, Gray-Milne Trust, 1940

Jordan, T.H.: Lateral heterogeneity and mantle dynamics. Nature **257**, 745–750, 1975

Jordan, T.H., Minster, J.B.: Application of a stochastic inverse to the geophysical inverse problem. In: Mathematics of profile inversion (L. Colin, ed.), pp. 7-36–7-47, NASA Technical Memorandum X-62150, 1972

Jordan, T.H., Lynn, W.S.: A velocity anomaly in the lower mantle. J. Geophys. Res. **79**, 2679–2685, 1974

Long, R.E., Mitchell, M.G.: Teleseismic P-wave delay time in Iceland. Geophys. J. Roy. Astr. Soc. **20**, 41–48, 1970

McKenzie, D.P.: Speculations on the causes and consequences of plate motions. Geophys. J. Roy. Astr. Soc. **18**, 1–32, 1969

McKenzie, D.P., Roberts, J.M., Weiss, N.O.: Convection in the earth's mantle: towards a numerical simulation. J. Fluid Mech. **62**, 465–538, 1974

Mitronovas, W., Isacks, B.L.: Seismic velocity anomalies in the upper mantle beneath the Tonga-Kermadec Island Arc. J. Geophys. Res. **76**, 7154–7180, 1971

National Oceans and Atmospheric Administration, U.S. Dept. Interior: Preliminary determination of epicenters, Denver, Colorado, 1971

O'Connell, R.J.: On the scale of mantle convection. Tectonophysics, in press, 1976

Powell, C.A.: Mantle heterogeneity: evidence from large seismic arrays. Ph.D. Thesis, Princeton Univ., 1976

Richter, R.M., Parsons, B.: On the interaction of two scales of convection. J. Geophys. Res. **80**, 2529–2541, 1975

Schubert, G., Yuen, D.A., Turcotte, D.L.: Role of phase transitions in a dynamic mantle. Geophys. J. Roy. Astr. Soc. **42**, 705–735, 1975

Sengupta, M.K.: The structure of the earth's mantle from body wave observations. Ph.D. Thesis, Mass. Inst. of Tech., 1975

Sipkin, S.A., Jordan, T.H.: Lateral heterogeneity of the upper mantle determined from the travel times of ScS. J. Geophys. Res. **80**, 1474–1484, 1975

Sipkin, S.A., Jordan, T.H.: Lateral heterogeneity of the upper mantle determined from the travel times of multiple ScS. J. Geophys. Res. **81**, 6307–6320, 1976

Sleep, N.H.: Teleseismic P-wave transmission through slabs. Bull. Seis. Soc. Am. **63**, 1349–1373, 1973

Toksöz, M.N., Minear, J.W., Julian, B.R.: Temperature field and geophysical effects of a downgoing slab. J. Geophys. Res. **76**, 1113–1138, 1971

Veith, K.F.: The relationship of island arc seismicity to plate tectonics. Ph.D. Thesis, S. Methodist Univ., 1974

Weichert, D.H.: Anomalous azimuths of P: evidence for lateral variations in the deep mantle. Earth Planet. Sci. Lett. **17**, 181–188, 1972

Received October 26, 1976; Revised Version February 3, 1977